Estimation of Oceanic Precipitation Efficiency in Cloud Models

CHUNG-HSIUNG SUI

Institute of Hydrological Sciences, and Department of Atmospheric Sciences, National Central University, Chung-Li, Taiwan

XIAOFAN LI

Joint Center for Satellite Data Assimilation, and NOAA/NESDIS/Office of Research and Applications, Camp Springs, Maryland

MING-JEN YANG

Institute of Hydrological Sciences, National Central University, Chung-Li, Taiwan

HSIAO-LING HUANG

Institute of Geography, Chinese Culture University, Taipei, Taiwan

(Manuscript received 22 June 2004, in final form 8 March 2005)

ABSTRACT

Precipitation efficiency is estimated based on vertically integrated budgets of water vapor and clouds using hourly data from both two-dimensional (2D) and three-dimensional (3D) cloud-resolving simulations. The 2D cloud-resolving model is forced by the vertical velocity derived from the Tropical Ocean Global Atmosphere Coupled Ocean–Atmosphere Response Experiment (TOGA COARE). The 3D cloud-resolving modeling is based on the fifth-generation Pennsylvania State University–National Center for Atmospheric Research (PSU–NCAR) Mesoscale Model (MM5) simulation of Typhoon Nari (in 2001). The analysis of the hourly moisture and cloud budgets of the 2D simulation shows that the total moisture source (surface evaporation and vertically integrated moisture convergence) is converted into hydrometeors through vapor condensation and deposition rates regardless of the area size where the average is taken. This leads to the conclusion that the large-scale and cloud-microphysics precipitation efficiencies are statistically equivalent. Results further show that convergence (divergence) of hydrometeors would make precipitation efficiency larger (smaller). The precipitation efficiency tends to be larger (even >100%) in light rain conditions as a result of hydrometeor convergence from the neighboring atmospheric columns. Analysis of the hourly moisture and cloud budgets of the 3D results from the simulation of a typhoon system with heavy rainfall generally supports that of 2D results from the simulation of the tropical convective system with moderate rainfall intensity.

1. Introduction

Precipitation is generated by convective processes that are unresolvable subgrid-scale eddies in global atmospheric models. As a result, various cumulus parameterization schemes have been designed to use the large-scale variables to estimate the amount of precipitation and the associated heating and moistening effects in atmospheric models. Frequently used cumulus parameterization schemes include the Kuo (1965, 1974), Arakawa–Schubert (Arakawa and Schubert 1974), Manabe–Strickler (Manabe and Strickler 1964), and Betts–Miller (Betts 1986; Betts and Miller 1986) schemes. In atmospheric regional models, convective processes still need to be parameterized, although prognostic cloud-microphysics parameterization may be included in the part of model domains of a finer spatial resolution. Cumulus parameterization schemes commonly used in the regional models include the Kain–Fritsch (Kain and Fritsch 1993), Grell (Grell 1993), and Betts–Miller schemes. The use of cumulus parameterizations in atmospheric regional and global models has

Corresponding author address: C.-H. Sui, Institute of Hydrological Sciences, National Central University, No. 300, Wu-Chuan Li, Chung-Li, Tao-Yuan, 320 Taiwan.
E-mail: sui@cc.ncu.edu.tw

led to many successes of simulations of atmospheric circulations.

However, the estimation of precipitation by diagnostic cumulus parameterization schemes has many limitations, like the need for closure assumptions. As a result, the model-predicted rainfall often contains large uncertainties. As computational power increases, prognostic cloud-microphysics parameterization schemes are employed in cloud-resolving mesoscale models, regional, and even global models. Willoughby et al. (1984) conducted an experiment with parameterized ice-phase cloud-microphysics using an axisymmetric, nonhydrostatic tropical cyclone model, and argued that widespread cooling associated with the melting of graupel in mesoscale downdrafts affected the formation of multiple convective rings and the development of a hurricane. Lord et al. (1984) further carried out a budget analysis that supported the hypothesis by Willoughby et al. (1984). Liu et al. (1997) carried out a multiscale numerical study of Hurricane Andrew (in 1992) using an improved version of the fifth-generation Pennsylvania State University–National Center for Atmospheric Research (PSU–NCAR) Mesoscale Model (MM5; Grell et al. 1994), and found that the inclusion of a microphysics parameterization scheme in the MM5 led to a more realistic simulation of hurricane cloud structures when compared to the observations.

While the atmospheric regional models are designed for studying synoptic-scale disturbances, cloud-resolving models are powerful tools for studying precipitation processes in convective and mesoscale systems. Through a systematic approach, we have investigated atmospheric water and energy cycles in a series of papers using a cloud-resolving model that contains prognostic microphysics parameterization schemes (Sui et al. 1994, 1998; Li et al. 1999, 2002a,b,c). In this study, we perform an analysis of cloud-microphysics budgets to study the processes determining precipitation efficiency, and the effect of hydrometeor convergence on precipitation efficiency.

In Li et al. (2002b), the large-scale precipitation efficiency (LSPE) was defined as the ratio of the surface rainfall rate to the sum of the surface evaporation and moisture convergence, and the cloud-microphysics precipitation efficiency (CMPE) as the ratio of the surface rainfall rate to the sum of the condensation and deposition rates of supersaturated vapor. The concept of LSPE was used by Kuo (1965, 1974) who assumed a fraction of total moisture source due to vertically integrated large-scale moisture convergence plus surface evaporation was consumed to produce precipitation. This CMPE is similar to the precipitation efficiency defined by Weisman and Klemp (1982) and Lipps and Hemler (1986). The domain-mean results of Li et al. (2002b) show that the LSPE could be more than 100% whereas the CMPE is less than 100%. Since the LSPE and CMPE are expected to be the same based on physical considerations, the difference in Li et al. (2002b) is attributed in the present study to the horizontal cloud advection that is excluded in the domain-mean CMPE due to the cyclic lateral boundary condition.

The above considerations lead us to ask several key questions. Are the CMPE and LSPE physically and statistically compatible? What processes determine precipitation efficiency? Is precipitation efficiency dependent on the strength of convection? The goal of this study is to answer the above questions using both two-dimensional (2D) and three-dimensional (3D) cloud-resolving models. The 2D model and forcing are discussed in section 2. The vertically integrated budgets of water vapor and clouds for 2D model are estimated in section 3. The importance of horizontal cloud advection in the prediction of surface rainfall rate in 2D model results is examined in section 4. The 2D results are supported by the analysis of a 3D typhoon simulation using a mesoscale model in section 5. A summary is given in section 6.

2. 2D cloud-resolving model and experiment

The Goddard Cumulus Ensemble (GCE) Model is used for this study. The GCE model is a cloud-resolving model originally developed by Soong and Ogura (1980), Soong and Tao (1980), Tao and Simpson (1993), and Tao et al. (1993). The 2D version of the model used by Sui et al. (1994, 1998) and further modified by Li et al. (1999) is used in this study. The governing equations with an anelastic approximation can be expressed as follows:

$$\frac{\partial u'}{\partial x} + \frac{1}{\overline{\rho}}\frac{\partial(\overline{\rho}w')}{\partial z} = 0, \tag{1}$$

$$\frac{\partial u'}{\partial t} = -\frac{\partial}{\partial x}(u'\overline{u}^o + \overline{u}^o u' + u'u') - \frac{1}{\overline{\rho}}\frac{\partial}{\partial z}\overline{\rho}(w'\overline{u}^o + \overline{w}^o u' + w'u' - \overline{w'u'}) - c_p\frac{\partial(\overline{\theta}\pi')}{\partial x} + D_u - \overline{D}_u, \tag{2}$$

$$\frac{\partial w'}{\partial t} = -\frac{\partial}{\partial x}(u'\overline{w}^o + \overline{u}^o w' + u'w') - \frac{1}{\overline{\rho}}\frac{\partial}{\partial z}\overline{\rho}(w'\overline{w}^o + \overline{w}^o w' + w'w' - \overline{w'w'}) - c_p\frac{\partial(\overline{\theta}\pi')}{\partial z} + g\left(\frac{\theta'}{\theta_b} + 0.61q_v' - q_l'\right) + D_w - \overline{D}_w, \quad (3)$$

$$\frac{\partial \theta}{\partial t} = -\frac{\partial(u'\theta')}{\partial x} - \overline{u}^o\frac{\partial\theta'}{\partial x} - \frac{1}{\overline{\rho}}\frac{\partial(\overline{\rho}w'\theta')}{\partial z} - \overline{w}^o\frac{\partial\theta'}{\partial z} - w'\frac{\partial\overline{\theta}}{\partial z} + \frac{1}{\pi c_p}Q_{\mathrm{cn}} + \frac{1}{\pi c_p}Q_R - \overline{u}^o\frac{\partial\overline{\theta}^o}{\partial x} - \overline{w}^o\frac{\partial\overline{\theta}}{\partial z} + D_\theta, \quad (4)$$

$$\frac{\partial q_v}{\partial t} = -\frac{\partial(u'q_v')}{\partial x} - \overline{u}^o\frac{\partial q_v'}{\partial x} - \frac{1}{\overline{\rho}}\frac{\partial(\overline{\rho}w'q_v')}{\partial z} - \overline{w}^o\frac{\partial q_v'}{\partial z} - w'\frac{\partial\overline{q}_v}{\partial z} - \overline{u}^o\frac{\partial\overline{q}_v^o}{\partial x} - \overline{w}^o\frac{\partial\overline{q}_v}{\partial z} - S_{qv} + D_{qv}, \quad (5)$$

$$\frac{\partial q_\chi}{\partial t} = -\frac{\partial(uq_\chi)}{\partial x} - \frac{1}{\overline{\rho}}\frac{\partial}{\partial z}\overline{\rho}(w - w_{\mathrm{TV}})q_\chi + S_{q\chi} + D_{q\chi}, \quad (6)$$

where a variable with an overbar denotes the zonal mean part of the variable and the corresponding deviation part of the variable is denoted with a prime. Subscript "b" denotes an initial value, which does not vary with time; superscript "o" denotes imposed observed variables in the model. In the above equations, u and w are zonal and vertical air wind components, respectively; θ and q_v are air potential temperature and specific humidity, respectively; $q_\chi = (q_c, q_r, q_i, q_s, q_g)$, q_c, q_r, q_i, q_s, q_g are the mixing ratios of cloud water (small cloud droplets), raindrops, cloud ice (small ice crystals), snow (density 0.1 g cm^{-3}), and graupel (density 0.4 g cm^{-3}), respectively; $\overline{\rho}$ is a mean air density, which is a function of height only; w_{TV} is a terminal velocity, which is zero for cloud water and ice; $\pi = (p/p_0)^\kappa$, $\kappa = R/c_p$, R is the gas constant; c_p is the specific heat of dry air at constant pressure p; and $p_o = 1000$ hPa. Here S_{qv} represents the source and sink terms of water vapor as described in the appendix in Li et al. (2002c); Q_{cn} denotes the net latent heat release through phase changes among different cloud species (see the appendix in Li et al. 2002c) that can be expressed symbolically as $L_v(c - e) + L_s(d - s) + L_f(f - m)$, where c, e, d, s, f, and m are condensation, evaporation, deposition, sublimation, fusion, and melting, respectively; L_v, L_s, and L_f are latent heat coefficients due to phase changes. Here Q_R is the radiative heating rate due to convergence of net flux of solar and infrared radiative fluxes; $S_{q\chi}$ is the source and sink of various hydrometeor species, which are parameterized by the schemes proposed by Hsie et al. (1980), Rutledge and Hobbs (1983, 1984), Lin et al. (1983), Tao et al. (1989), and Krueger et al. (1995) [see Li et al. (1999, 2002c) for cloud budget equations and comprehensive discussions]; and, finally, D's are turbulent dissipation terms.

The 2D model is forced by the zonally uniform vertical velocity, zonal wind, and thermal and moisture advections, which are derived by M. Zhang and his research group at the State University of New York at Stony Brook, New York, based on the 6-hourly observations from the Tropical Ocean Global Atmosphere Coupled Ocean–Atmosphere Response Experiment (TOGA COARE) within the Intensive Flux Array (IFA) region (M. Zhang 1999, personal communication). The calculations are based on the constrained variational method on column-integrated budgets of mass, heat, moisture, and momentum proposed by Zhang and Lin (1997). Hourly sea surface temperature at the Improved Meteorological (IMET) surface mooring buoy (1.75°S, 156°E; Weller and Anderson 1996) is also imposed in the model. The model is integrated from 0400 local standard time (LST) 19 December 1992 to 0400 LST 9 January 1993 (21 days total). In this 2D model setup, the horizontal domain is 768 km with a lateral cyclic boundary condition. The horizontal grid mesh is 1.5 km. The vertical grid resolution ranges from about 200 m near the surface to about 1 km about 100 hPa. The time step is 12 s.

The time evolution of the vertical distribution of the large-scale vertical velocity and zonal wind during 19 December 1992–9 January 1993 can be found in Li et al. (2002b; see their Fig. 1). During this period, the diurnal and 2-day variations are embedded in the developing intraseasonal oscillation in the first 10 days and the westerly wind burst event in the following 10 days over the TOGA COARE IFA. The maximum magnitude of vertical velocity is about 8 cm s^{-1} at 300–400 hPa. Maximum westerly wind can reach 12–16 m s^{-1} associated with weak descending motion.

Figure 1 shows the time evolution and horizontal distribution of simulated surface rainfall rate for the period of 0000 LST 20 December–1200 LST 21 December 1992 (36 h total). The rainbands propagated westward before 2000 LST 20 December 1992 and then started to propagate eastward. The change of propagation direction of the rainbands resulted from an intensification of lower-tropospheric westerly winds and a weakening of midtropospheric easterly winds (see Fig. 1 in Li et al.

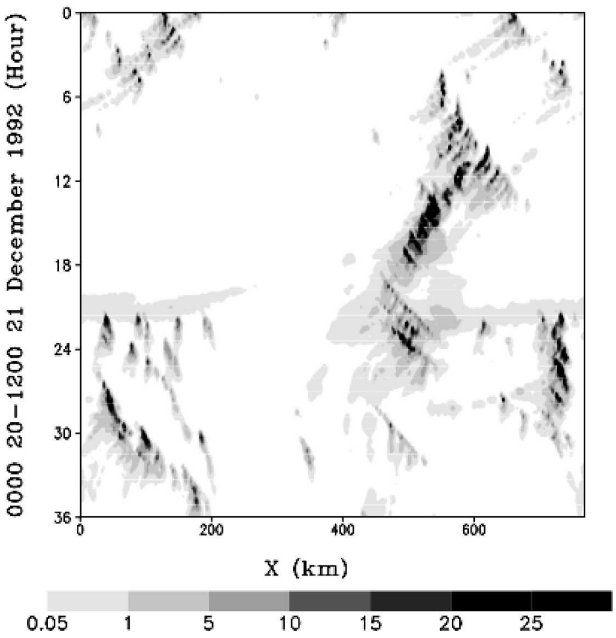

FIG. 1. Time evolution and horizontal distribution of surface rainfall rate (mm h^{-1}) simulated during 0000 LST 20 Dec–1200 LST 21 Dec 1992.

2002b). An analysis of the hourly simulation data within this 36-h period (0000 LST 20 December–1200 LST 21 December 1992) is presented in the current study. The same analysis is also applied to the hourly data of the 21-day period, and the conclusion remains unchanged.

3. Vertically integrated budgets of water vapor and clouds

The vertically integrated water vapor and total cloud budgets can be expressed as

$$\frac{\partial[q_v]}{\partial t} = [\mathrm{CONV}_{qv}] + E_s - [S_{qv}], \tag{7}$$

$$\frac{\partial[C]}{\partial t} = [\mathrm{CONV}_C] - P_s + [S_C], \tag{8}$$

where a term in square brackets signifies a vertically integrated quantity as defined by $[F] = \int_0^{z_t} \bar{\rho}\, F\, dz$ for any variable F, and z_t is the model top. In (7), q_v is the mixing ratio of water vapor, $[\mathrm{CONV}_{qv}]$ is moisture convergence, $E_s = \bar{\rho}\,(w'q_v')_s$ is surface evaporation, S_{qv} is the source and sink in the water vapor budget due to conversions between water vapor and various hydrometeor species. Here S_{qv} can be expressed in the two terms as

$$S_{qv} = \mathrm{SI}_{qv} - \mathrm{SO}_{qv}, \tag{9}$$

where $\mathrm{SI}_{qv} = [P_{\mathrm{CND}}] + [P_{\mathrm{DEP}}] + [P_{\mathrm{SDEP}}] + [P_{\mathrm{GDEP}}]$ represents the sink term in water vapor budget that consists of vapor condensation rate ($[P_{\mathrm{CND}}]$), vapor deposition rates for growth of cloud ice ($[P_{\mathrm{DEP}}]$), snow ($[P_{\mathrm{SDEP}}]$) and graupel ($[\mathrm{P}_{\mathrm{GDEP}}]$), and $\mathrm{SO}_{qv} = [P_{\mathrm{REVP}}] + [P_{\mathrm{MLTG}}] + [P_{\mathrm{MLTS}}]$ represents the source term consisting of growth of vapor by evaporation of raindrops ($[P_{\mathrm{REVP}}]$), melting graupel ($[P_{\mathrm{MLTG}}]$), and melting snow ($[P_{\mathrm{MLTS}}]$).

In (8), C is the sum of mixing ratios of cloud water (q_c), raindrops (q_r), cloud ice (q_i), snow (q_s), and graupel (q_g); $[\mathrm{CONV}_C]$ is the hydrometeor convergence; $P_s = \bar{\rho}\,(w_{\mathrm{TV}}C)_s$ is the surface rainfall rate; w_{TV} is the terminal velocity of each cloud species; and $S_C = S_{qv}$. Note that when averaged over the whole domain under the cyclic boundary condition in this study, $[\mathrm{CONV}_C] = 0$ whereas $[\mathrm{CONV}_{qv}] = -[\overline{u}^o(\partial\overline{q}_v^o/\partial x)] - [\overline{w}^o(\partial\overline{q}_v/\partial z)]$, due to the imposed zonally uniform forcing calculated from the observation data.

To first examine the dominant terms in the cloud budget equations, we show the time- and domain-mean cloud-microphysics budgets in Fig. 2. The time interval is 36 h. The domain includes the entire horizontal area and vertical depth of the model domain. The budget shows that most of the moisture sources form cloud water and cloud ice through vapor condensation ($P_{\mathrm{CND}} = 0.83$ mm h^{-1}) and deposition ($P_{\mathrm{DEP}} = 0.14$ mm h^{-1}). The conversion of cloud water to precipitation occurs primarily through the collection of cloud water by rain below the freezing level ($P_{\mathrm{RACW}} = 0.55$ mm h^{-1}) and through riming of cloud water onto precipitating ice (snow and graupel) above the freezing level ($P_{\mathrm{GACW}} + P_{\mathrm{SACW}} = 0.26$ mm h^{-1}). The melting of precipitating ice ($P_{\mathrm{GMLT}} = 0.4$ mm h^{-1}) mainly compensates the evaporation of rain ($P_{\mathrm{REVP}} = 0.36$ mm h^{-1}). The collection efficiency ($P_{\mathrm{RACW}}/P_{\mathrm{CND}} = 66\%$) accounts for the precipitation efficiency [$P_s/(P_{\mathrm{CND}} + P_{\mathrm{DEP}}) = 67\%$].

To further examine the relation between the moisture sources and microphysical processes, we examine the hourly averaged values of SI_{qv} versus the total moisture source (the sum of surface evaporation and $[\mathrm{CONV}_{qv}]$) as shown in Fig. 3. The hourly budgets are averaged in three grid area sizes of 96, 48, and 24 km in the 2D framework, respectively, in order to examine the area dependence of the relationship. The figure shows that the two variables have very similar variations, independent of the grid area sizes. The root-mean-square differences between the two variables are less than 1.3, 1.8, and 2.5 mm h^{-1} for the 96-, 48-, and 24-km averages, respectively, and their linear correlation coefficients are about 0.89 for all the three cases, which is well above the 99% confidence level. The linear regression equations can be expressed by

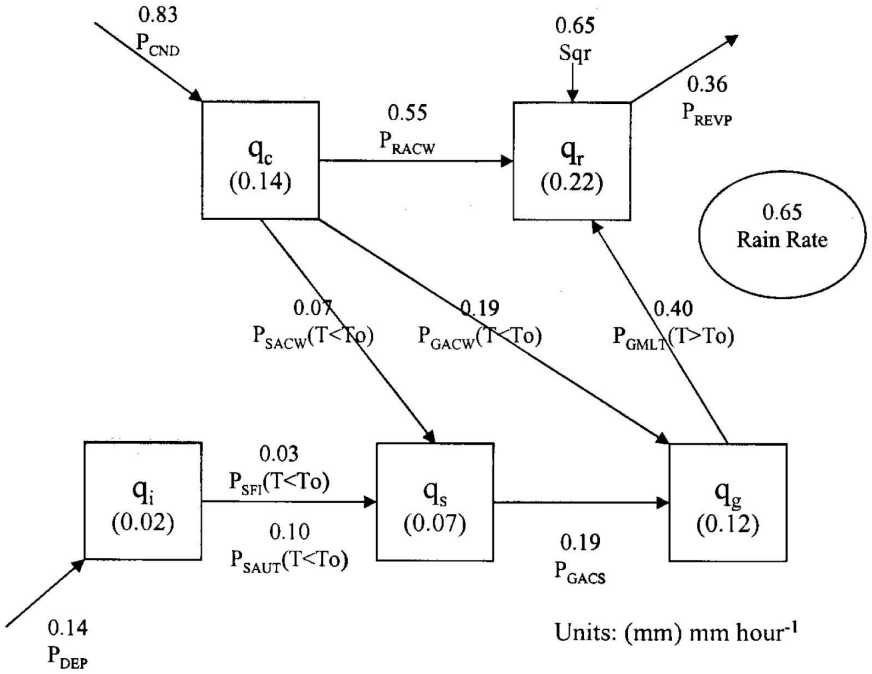

FIG. 2. The 36-h-averaged and zonal-mean cloud-microphysics budgets simulated during 0000 LST 20 Dec–1200 LST 21 Dec 1992. Units for cloud hydrometeors and conversion rates are mm and mm h^{-1}, respectively.

$$\mathrm{SI}_{qv} = A_1 + B_1 \times (E_s + [\mathrm{CONV}_{qv}]), \tag{10}$$

where A_1 and B_1 are constant coefficients. The constant coefficients A_1 and B_1 are -0.1 and 1.2 for 96-km averages, -0.1 and 1.1 for 48-km averages, and -0.1 and 1 for 24-km averages, respectively. Thus, $\mathrm{SI}_{qv}/(E_s + [\mathrm{CONV}_{qv}])$ are 1.2 for 96-km averages, 1.1 for 48-km averages, and 1 for 24-km averages, respectively. The statistic calculations suggest that

$$[P_{\mathrm{CND}}] + [P_{\mathrm{DEP}}] + [P_{\mathrm{SDEP}}] + [P_{\mathrm{GDEP}}] \approx E_s + [\mathrm{CONV}_{qv}] \tag{11}$$

be a valid approximation, in particular, for the 24-km averages.

4. Precipitation efficiency

Equation (11) supports the basic premise of Kuo's (1965, 1974) cumulus parameterization. However, what portion of the net vapor condensation and deposition rate converts into surface rainfall rate is central to the cumulus parameterization. This can be expressed by "precipitation efficiency." Here, we introduce two definitions of precipitation efficiency. One is the CMPE:

$$\mathrm{CMPE} = \frac{P_s}{[\mathrm{SI}_{qv}]} = 1 - \frac{[\mathrm{SO}_{qv}]}{[\mathrm{SI}_{qv}]} + \frac{[\mathrm{CONV}_C]}{[\mathrm{SI}_{qv}]}. \tag{12}$$

In (12), the storage term of clouds is negligible. The CMPE is defined as the ratio of surface rainfall rate to the sum of vapor condensation rate, that is, the vapor deposition rate for growth of cloud ice, snow, and graupel (SI_{qv}). Notice that the CMPE defined here is different from that defined in Li et al. (2002b), since additional terms ($[P_{\mathrm{SDEP}}] + [P_{\mathrm{GDEP}}]$) may be important for mesoscale calculations. Also note that CMPE > 1 occurs when the hydrometeor convergence is greater than vapor growth rate by evaporation of raindrop and melting graupel/snow (i.e., $[\mathrm{SO}_{qv}] < [\mathrm{CONV}_C]$).

The other is the LSPE:

$$\mathrm{LSPE} = \frac{P_s}{[\mathrm{CONV}_{qv}] + E_s} = \frac{P_s}{[\mathrm{SI}_{qv}] - [\mathrm{SO}_{qv}] + \partial[q_v]/\partial t}. \tag{13}$$

The LSPE is defined as the ratio of surface rainfall rate to the sum of surface evaporation and vertically integrated horizontal and vertical moisture advection. The LSPE defined here is identical to the LSPE in Li et al. (2002b) when the LSPE is calculated using domain-mean quantities.

From physical considerations, the two precipitation efficiencies should be the same regardless of different definitions. Comparing Eqs. (11), (12), and (13), the two definitions are consistent, that is, the CMPE and

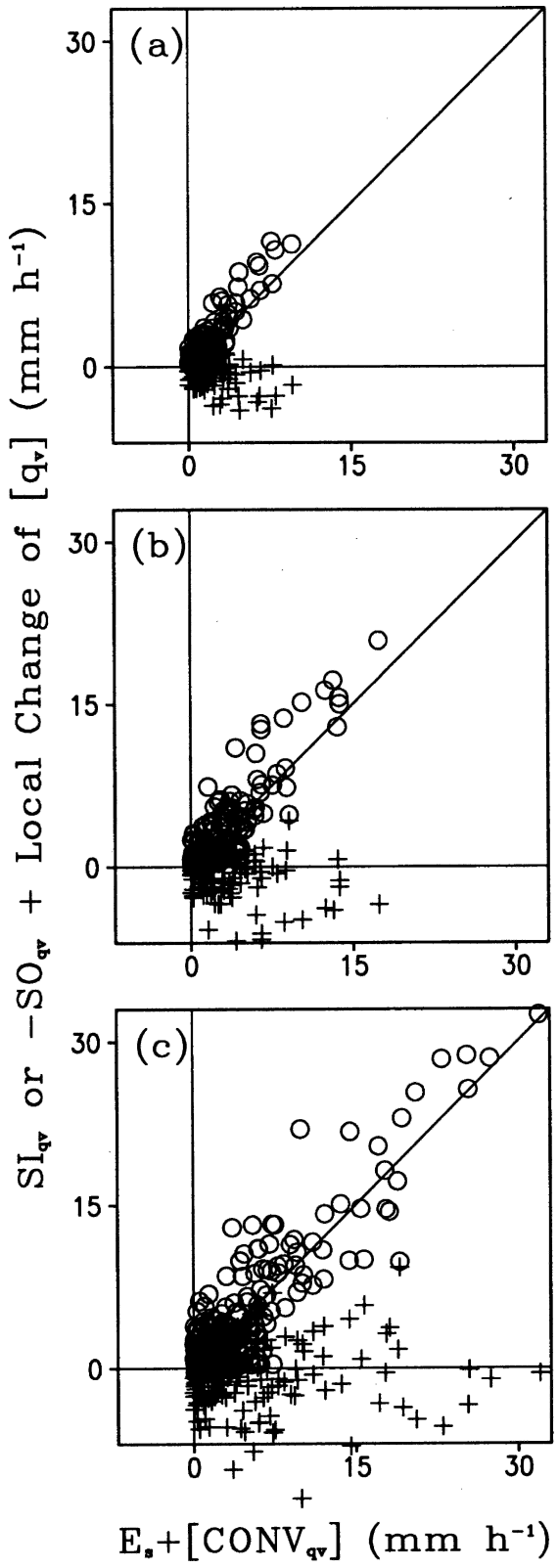

FIG. 3. Here $[SI_{qv}]$ (circle) and $-[SO_{qv}] + \partial[q_v]/\partial t$ (cross) vs $E_s + [CONV_{qv}]$ averaged within (a) 96, (b) 48, and (c) 24 km (mm h^{-1}). The diagonal lines denote $E_s + [CONV_{qv}] = [SI_{qv}]$.

LSPE are expected to be equivalent statistically. The three equations also imply that the magnitudes of $[SO_{qv}] - \partial[q_v]/\partial t$ to be statistically much smaller than the magnitude of $[SI_{qv}]$. To examine the validity of this relation, we compare the hourly mean values of $[SO_{qv}] - \partial[q_v]/\partial t$ with those of $[SI_{qv}]$ and $[CONV_{qv}] + E_s$ in Fig. 3. To examine whether the relation is sensitive to the area size where the average is taken, the relation is compared in three grid area sizes (96, 48, and 24 km). Indeed, the figure indicates that magnitudes of $[SO_{qv}] - \partial[q_v]/\partial t$ are statistically much smaller than the magnitude of $[SI_{qv}]$. This is consistent with the finding that the sum of vapor condensation rate, vapor deposition rates for growth of cloud ice, snow, and graupel (SI_{qv}) approximately equals the sum of surface evaporation and vertically integrated horizontal and vertical moisture advection. As a result, the CMPE and LSPE are statistically interchangeable as indicated in Fig. 4. The linear correlation coefficients between CMPE and LSPE are 0.55 for all the three area averages, which is well above the 99% confidence level. The linear regression equations can be expressed by

$$\text{LSPE} = A_2 + B_2\,\text{CMPE}, \tag{14}$$

where A_2 and B_2 are constant coefficients. The constant coefficients A_2 and B_2 are 5 and 1.25 for 96-km averages, 21.9 and 0.78 for 48-km averages, and 12.9 and 0.83 for 24-km averages, respectively. Thus, LSPE/CMPE are about 1.25 for 96-km averages, 0.78 for 48-km averages, and 0.83 for 24-km averages, respectively. Note that LSPE could be 100%–300% when CMPE is smaller than 100%. The LSPEs of larger than 100% occur, when $P_s < 5$ mm h^{-1} for 96- and 48-km averages and $P_s < 10$ mm h^{-1} for 24-km averages (not shown). This is caused by the local reduction of vapor with a small vapor source ($E_s + [CONV_{qv}]$).

It is also clear from Eqs. (12) and (13) that whether the LSPE is greater or smaller than the CMPE depends on the relative magnitude between $[SO_{qv}]$ and $\partial[q_v]/\partial t$. For the condition that the vapor growth rate by evaporation of raindrops and melting snow/graupel is larger than the time rate change of vapor (i.e., $[SO_{qv}] - \partial[q_v]/\partial t > 0$), such as over tropical stratiform precipitation clouds and the typhoon's spiral rainbands, the LSPE is greater than the CMPE. On the other hand, the LSPE is less than the CMPE when $[SO_{qv}] - \partial[q_v]/\partial t < 0$.

Doswell et al. (1996) proposed to calculate the precipitation efficiency using the data over the life span of a precipitation-producing weather system. Ferrier et al. (1996) and Tao et al. (2004) also computed precipitation efficiencies using 3- and 6-h-averaged simulation data, respectively. The LSPE calculated with the 36-h-averaged zonal-mean simulated data is about 100%,

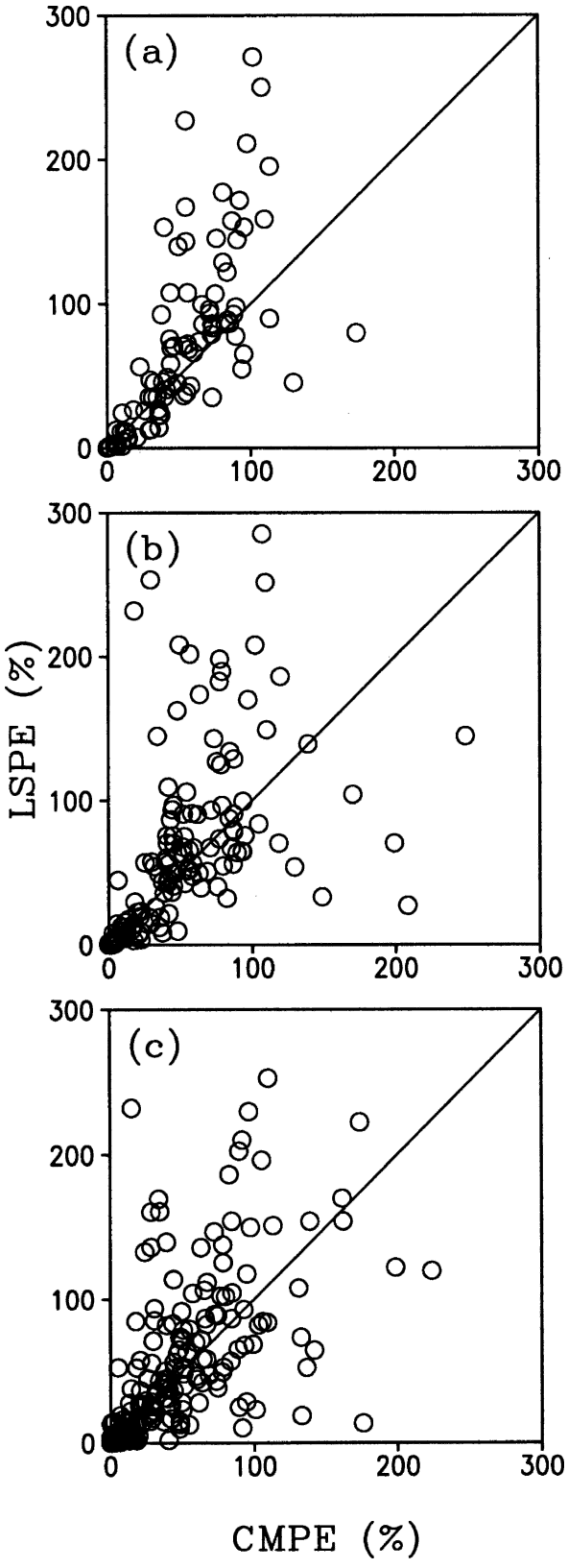

FIG. 4. Here LSPE vs CMPE averaged within (a) 96, (b) 48, and (c) 24 km. Unit is %. The diagonal lines denote LSPE = CMPE.

which includes several life spans of tropical convections as indicated in Fig. 1. This suggests that almost all the environmental vapor sources are consumed by the precipitation during the strong convective development. The relation that the 36-h-averaged zonal-mean LSPE $\approx 100\%$ can be demonstrated by adding (7) and (8) and taking the zonal mean. The combined equation becomes

$$\frac{\partial[\overline{q_v}]}{\partial t} + \frac{\partial[\overline{C}]}{\partial t} = [\overline{\mathrm{CONV}_{qv}}] + E_s - P_s, \qquad (15)$$

where $[\overline{\mathrm{CONV}_C}] = 0$ due to the cyclic boundary condition. The long-term time average (e.g., 36-h average here) of (15) is

$$[\overline{\mathrm{CONV}_{qv}}] + E_s - P_s \approx 0, \qquad (16)$$

where $\partial[\overline{q_v}]/\partial t \approx 0$, and $\partial[\overline{C}]/\partial t \approx 0$. Equation (16) indicates that the 36-h-averaged zonal-mean LSPE $\approx$ 100%. The 36-h-averaged zonal-mean CMPE is 63.5%, which is smaller than the corresponding LSPE. Taking 36-h-averaged zonal mean on (7), (7) becomes

$$[\overline{\mathrm{CONV}_{qv}}] + E_s \approx \overline{\mathrm{SI}_{qv}} - \overline{\mathrm{SO}_{qv}}, \qquad (17)$$

where $\partial[\overline{q_v}]/\partial t \approx 0$. Since the evaporation rate of raindrops (P_{REVP}) determines SO_{qv}, which is always positive, $[\overline{\mathrm{CONV}_{qv}}] + E_s < \overline{\mathrm{SI}_{qv}}$, which causes that CMPE $<$ LSPE for the calculations with the 36-h-averaged zonal-mean simulation data.

The CMPE provides a basis for identifying the relevant processes determining precipitation efficiency. It is obvious from (11) that the positive values of $[\mathrm{CONV}_C]$ make CMPE larger through the advection of clouds into the region of interest, while negative values of $[\mathrm{CONV}_C]$ make CMPE smaller. This is indeed observed in the plot of hydrometeor convergence versus CMPE (Fig. 5), indicating that the larger CMPEs are associated with hydrometeor convergence while smaller CMPE*s* are associated with hydrometeor divergence. Depending on the relative magnitude between $[\mathrm{SO}_{qv}]$ and $[\mathrm{CONV}_C]$ in (12), CMPE could be even larger than 1 if $[\mathrm{CONV}_C] > [\mathrm{SO}_{qv}]$. Indeed in Fig. 5 it is shown that there are many cases of CMPE $> 100\%$. The above results indicate a significant effect of hydrometeor convergence on surface precipitation distribution.

Since the hydrometeor convergence is expected to be a function of the strength of convection, we further examine the dependence of CMPE on the rainfall rate. Figure 6 shows the CMPE as a function of the surface rainfall rate averaged in three grid area sizes of 96, 48, and 24 km. The figure shows that CMPE values spread

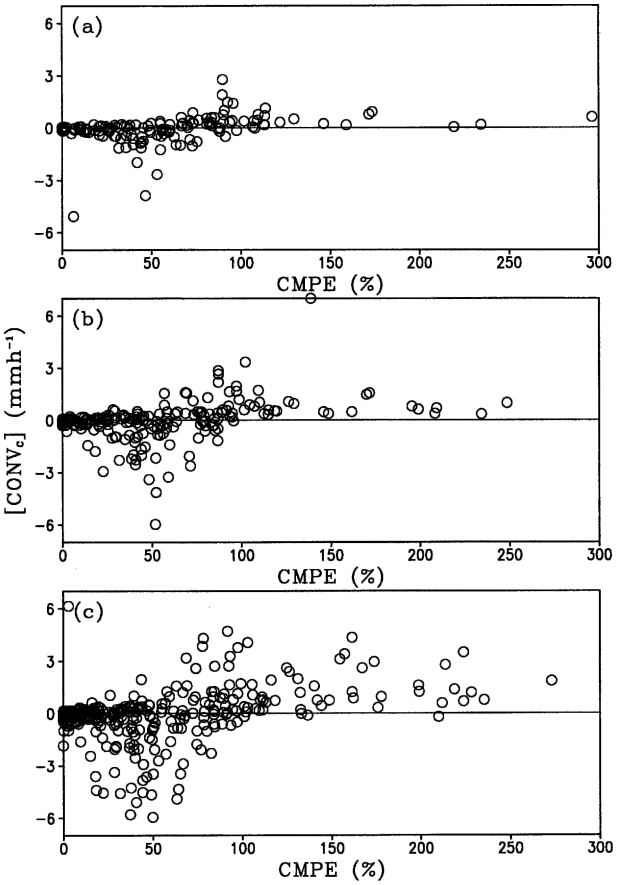

FIG. 5. Here [CONV$_C$] (mm h^{-1}) vs CMPE (%) averaged within (a) 96, (b) 48, and (c) 24 km.

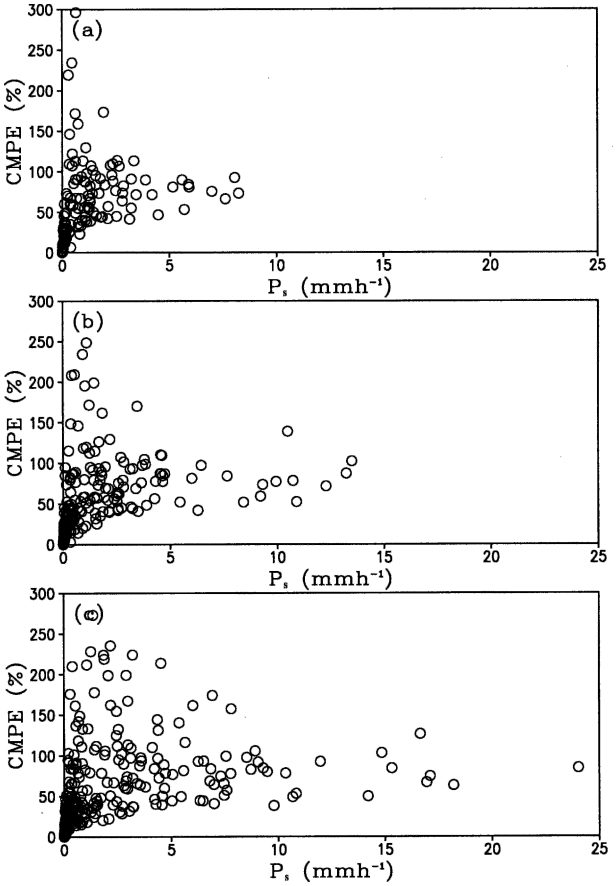

FIG. 6. Here CMPE (%) vs P_s (mm h^{-1}) averaged within (a) 96, (b) 48, and (c) 24 km.

over a wide range and become even larger than 100% in light rain conditions (i.e., the surface rainfall rates are smaller than 5 mm h^{-1} for 96- and 48-km averages and smaller than 10 mm h^{-1} for a 24-km average). But the CMPE tends to converge to a threshold value with increasing surface rainfall rate.

The above results clearly indicate that values of CMPE larger than 100% represent those cases with the surface rainfall rate larger than the total vapor condensation and deposition rates. This requires a positive hydrometeor convergence to balance the cloud budget [see Eq. (8) above]. Such a condition generally occurs in light rain conditions. In heavy rain situations, net condensation dominates and the effect of hydrometeor convergence becomes secondary.

5. Calculations from a three-dimensional typhoon simulation

To verify the conclusions made in the previous section, it is necessary to perform a similar examination of cloud-microphysics and vapor budgets from a more vibrant convection event. Here we examine results of a 3D simulation of Typhoon Nari (Yang and Huang 2004). The MM5 model is used to simulate the Typhoon Nari (in 2001). Nari brought more than 2000 mm of rain in 2 days over northern Taiwan, which caused widespread flooding and severe damage (Sui et al. 2002). The MM5 configuration includes four nested grids with horizontal grid sizes of 60, 20, 6.67, and 2.22 km, respectively, and 31 σ levels are used in the vertical on all four grids. The precipitation parameterizations used in the MM5 are the Grell (1993) cumulus scheme for subgrid-scale processes and the Reisner et al. (1998) microphysics scheme (graupel included) for explicit-scale processes. Note that the diagnostic cumulus parameterization scheme (Grell 1993) is not used on the 6.67- and 2.22-km grids. The MM5 with a 2.22-km grid size simulated the maximum 24-h rainfall of 856 mm near Mount Snow (over northern Taiwan) on 17 September 2001, in close agreement with the observed maximum of 940 mm (see Fig. 1 in Yang and Huang

2004). More details of the MM5 simulation of Typhoon Nari are given in Yang and Huang (2004) and will be reported in a series of forthcoming articles.

The horizontal distribution of simulated hourly surface rainfall rate (P_s) of Typhoon Nari on the 2.22-km grid averaged from 0300 to 0600 UTC 16 September 2001 is shown in Fig. 7a, which illustrates very intense precipitation (maximum $P_s \sim 75$ mm h^{-1}) within the eyewall, trailing stratiform rainfall in spiral rainbands, and convective showers over the mountain slopes. The corresponding CMPE and LSPE are shown in Figs. 7b,c. The two fields resemble each other over the ocean where the precipitation efficiency possesses the following features. It is generally less than 100% within the typhoon eyewall where rainfall is strongest, and exceeds 100% in many parts of the moderately raining spiral rainbands, where $[\text{CONV}_C]/[\text{SI}_{qv}] > [\text{SO}_{qv}]/[\text{SI}_{qv}]$ as shown in Figs. 7d,e. For these ocean points, the magnitudes of $[\text{SO}_{qv}] - \partial[q_v]/\partial t$ (see the cross points in Fig. 8) are statistically much smaller than the magnitude of $[\text{SI}_{qv}]$ (see the circle points in Fig. 8) for three averaged grid areas, which is consistent with the 2D results shown in Fig. 3.

Over the mountain areas in northern Taiwan, the patterns of CMPE and LSPE are dominated by northeast–southwest-oriented bands, quite different from the spiral structure over the ocean. The banded structure is more evident in the $[\text{CONV}_C]$ field as shown in Figs. 7e,f, indicative of gravity waves induced by the Central Mountain Range. The intense divergence fields associated with gravity waves causes a decoupling of CMPE from LSPE, such that the statistical balance of (11) is invalid (figure not shown). Over the mountain areas, $[\text{CONV}_C]$ dominates the cloud budget (cf. Figs. 7d,e,f), and the magnitude of CMPE is statistically larger than that of LSPE. The cloud-microphysical processes in the mountainous regions are complicated. A more thorough analysis is being analyzed and will be reported in a separate paper.

The CMPE and LSPE are further compared in the scatterplot averaged within three average grid areas as shown in Fig. 9. The three average areas are 118 km^2 (24 points on the 2.22-km grid), 59 km^2 (12 points on the 2.22-km grid), and 30 km^2 (6 points on the 2.22-km grid), respectively. Again, results are for ocean points only. The results show that the CMPE and LSPE are positively correlated (correlation coefficients 0.89, 0.86, and 0.79 for the 118, 59, and 30 km^2 average areas, respectively). The constant coefficients A_2 and B_2 of the linear regression Eqs. (14) are 2.25 and 1.02 for 118-km^2 averages, 3.29 and 0.98 for 59-km^2 averages, and 4.98 and 0.90 for 30-km^2 averages, respectively. Thus, LSPE/CMPE are about 1.02 for 118-km^2 averages, 0.98 for 59-km^2 averages, and 0.90 for 30-km^2 averages, respectively, consistent with the previous conclusion from a 2D simulation of a tropical convective system.

Figure 10 displays the relationship between $[\text{CONV}_C]$ and CMPE calculated from the 3D simulation of Typhoon Nari. Consistent with the feature in Fig. 5, larger values of CMPE in Fig. 9 are most likely associated with hydrometeor convergence while larger values of hydrometeor divergence are associated with smaller CMPE, again supporting the conclusion reached based on the previous 2D model results.

Figure 11 further shows the relationship between CMPE and P_s from the 3D simulation of Typhoon Nari. The figure indicates values of CMPE are scattered corresponding to lighter rainfall rates (<20 mm h^{-1}) but confined within a narrower range for heavier rainfall rates. The largest values of CMPE are associated with light rainfall rates. These characteristics are evident for all three average areas. Thus, the 3D simulation generally supports the previous conclusion.

6. Conclusions and discussions

In this study, we use the 2D cloud-resolving simulation of a tropical convection system and the 3D cloud-resolving simulation of a typhoon event to determine the precipitation efficiency from either the large-scale perspective or the cloud-microphysics perspective as in Li et al. (2002b). The focus is to better understand the processes that affect the precipitation efficiency. The 2D cloud-resolving model is used to simulate tropical convective systems with the imposed forcing from the TOGA COARE. The 3D cloud-resolving domain is nested in the MM5 to explicitly simulate heavy rainfalls associated with Typhoon Nari (in 2001).

The analysis of 2D results through the root-mean-square differences and linear correlation coefficients shows that the sum of vapor condensation rate (P_{CND}), vapor deposition rates for growth of cloud ice (P_{DEP}), snow (P_{SDEP}), and graupel (P_{GDEP}) is approximately balanced by the sum of surface evaporation (E_s) and vertically integrated moisture convergence (CONV_{qv}). This indicates that the total moisture source in the atmospheric column is converted into clouds, which is a basis of the Kuo (1965, 1974) cumulus parameterization scheme. This relation leads to the statistical equivalence of precipitation efficiency defined by the cloud-microphysics budget [$\text{CMPE} = P_s/(P_{\text{CND}} + P_{\text{DEP}} + P_{\text{SDEP}} + P_{\text{GDEP}})$] and that by total moisture source [$\text{LSPE} = P_s/(E_s + \text{CONV}_{qv})$], where P_s is the surface rainfall rate.

Analysis of the 2D simulation further shows that the

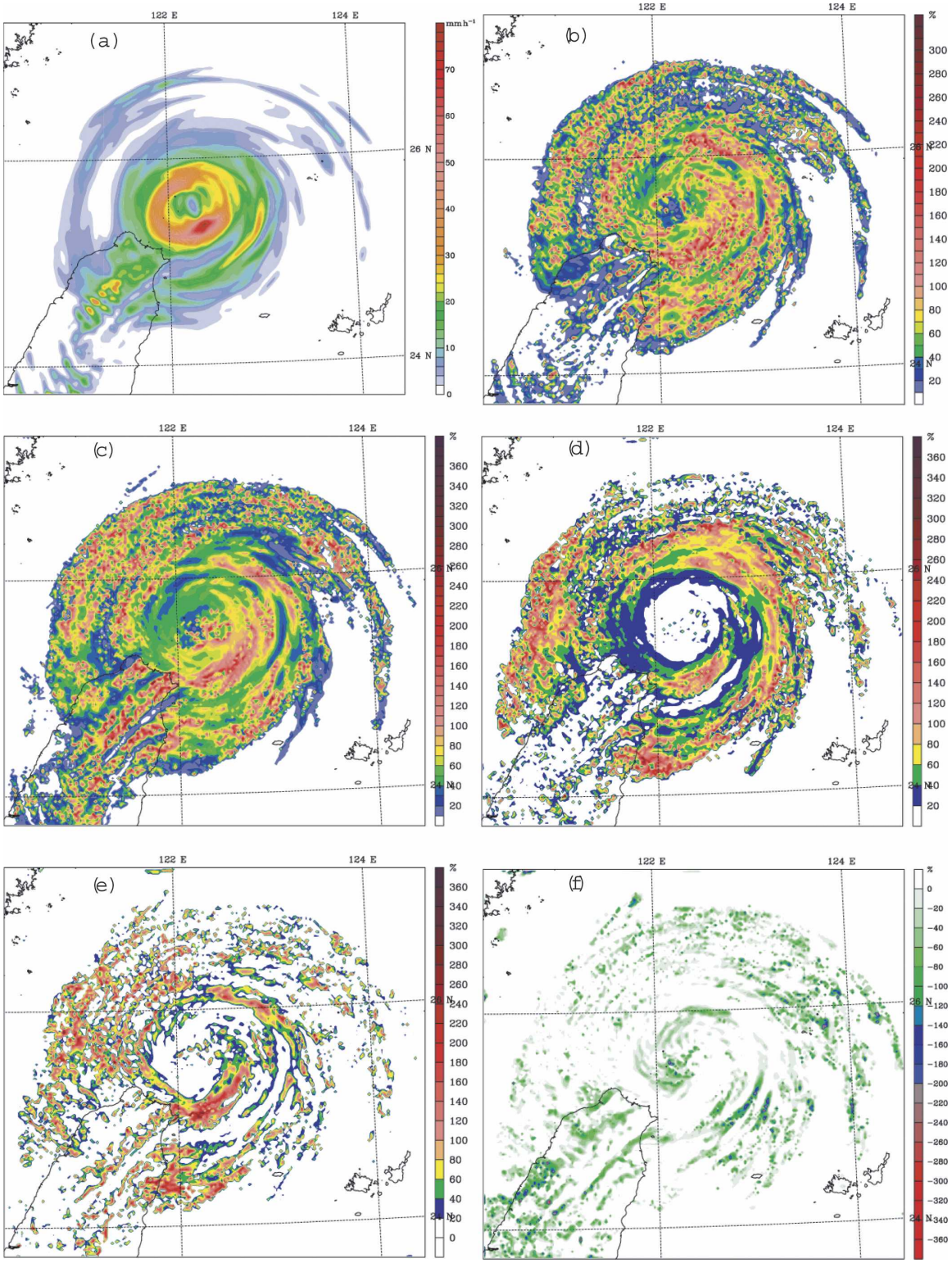

FIG. 7. The horizontal distribution of simulated (a) surface rain rate (mm h^{-1}), (b) LSPE, (c) CMPE, (d) $[SO_{qv}]/[SI_{qv}]$, (e) positive $[CONV_C]/[SI_{qv}]$, and (f) negative $[CONV_C]/[SI_{qv}]$ of Typhoon Nari averaged from 0300 to 0600 UTC 16 Sep 2001 on the 2.22-km grid. Values of (b)–(f) are averages of the 3-hourly budget estimates.

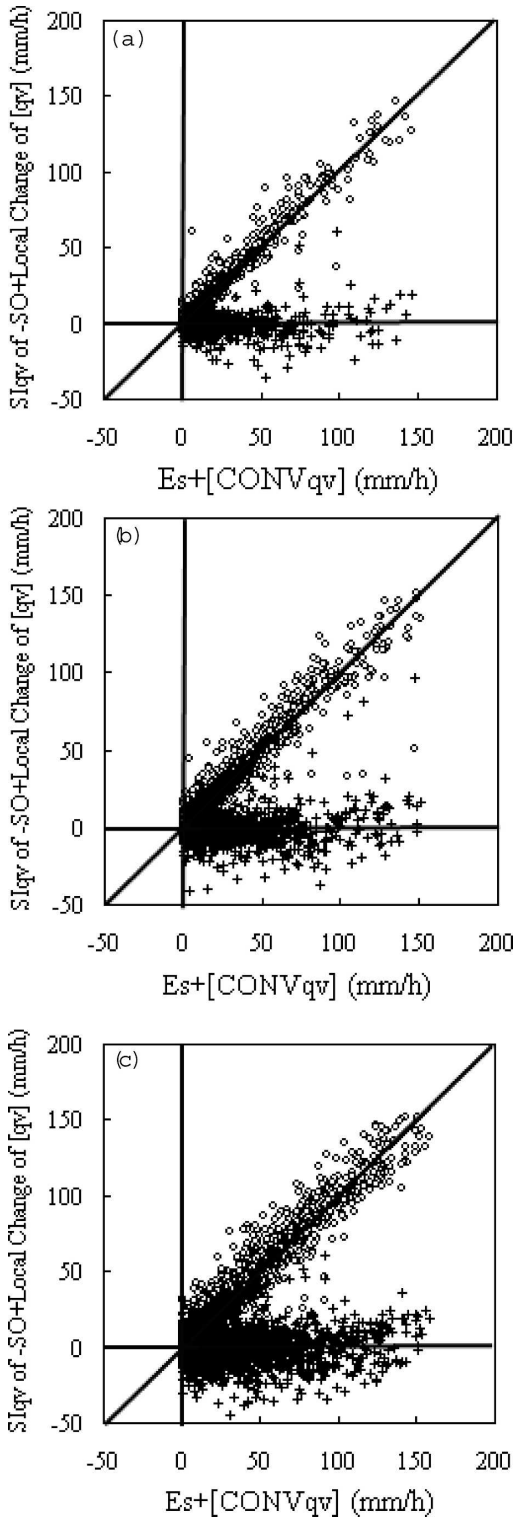

FIG. 8. Same as in Fig. 3 but for the MM5 simulation of Typhoon Nari averaged within $[SI_{qv}]$ (circle) and $-[SO_{qv}] + \partial[q_v]/\partial t$ (cross) vs $E_s + [CONV_{qv}]$ averaged within (a) 118 km^2 (24 points), (b) 59 km^2 (12 points), and (c) 30 km^2 (6 points). Results are for ocean points only. Unit is mm h^{-1}. The diagonal lines denote $E_s + [CONV_{qv}] = [SI_{qv}]$.

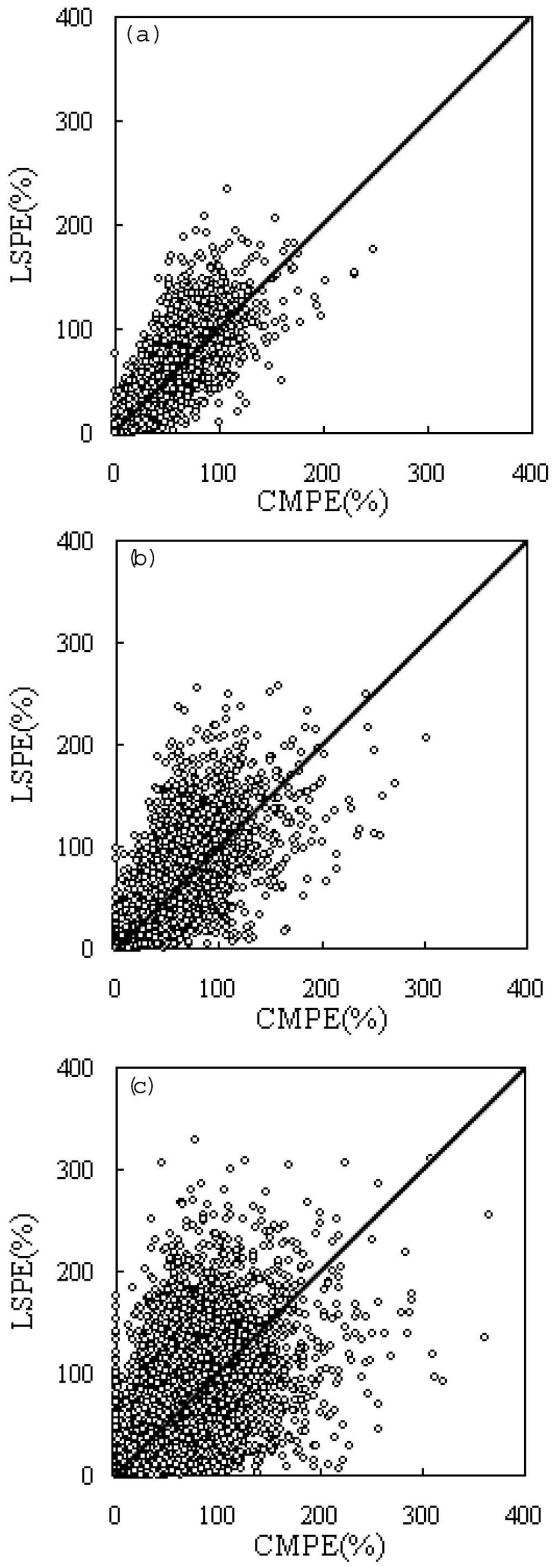

FIG. 9. Same as in Fig. 4 but for the MM5 simulation of Typhoon Nari (in 2001) averaged within (a) 118 km^2 (24 points), (b) 59 km^2 (12 points), and (c) 30 km^2 (6 points). Results are for ocean points only. The diagonal lines denote LSPE = CMPE.

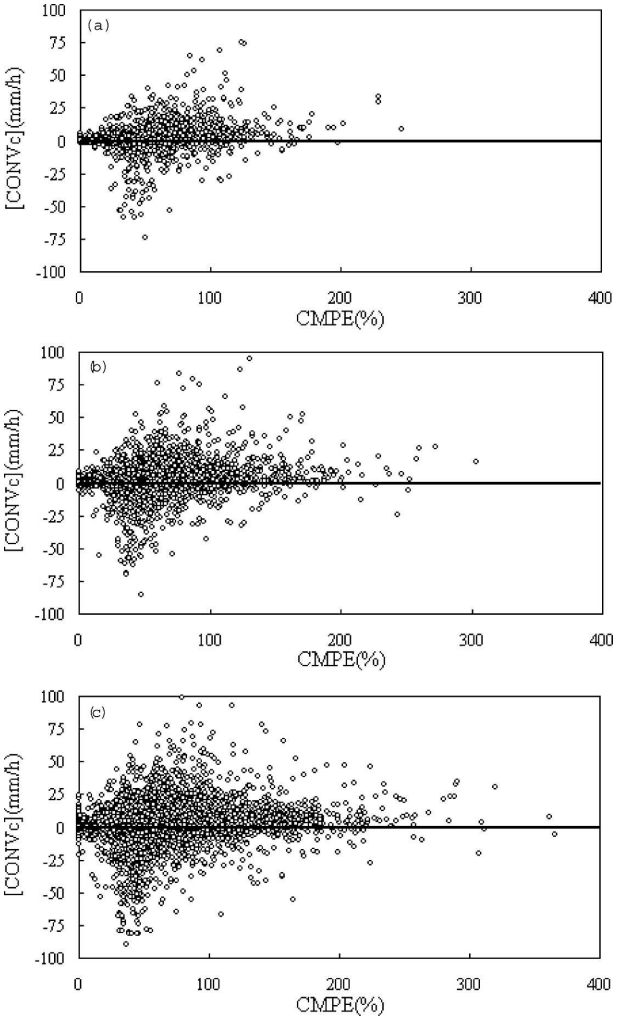

FIG. 10. Same as in Fig. 5 but for the MM5 simulation of Typhoon Nari (in 2001) averaged within (a) 118 km^2 (24 points), (b) 59 km^2 (12 points), and (c) 30 km^2 (6 points). Results are for ocean points only.

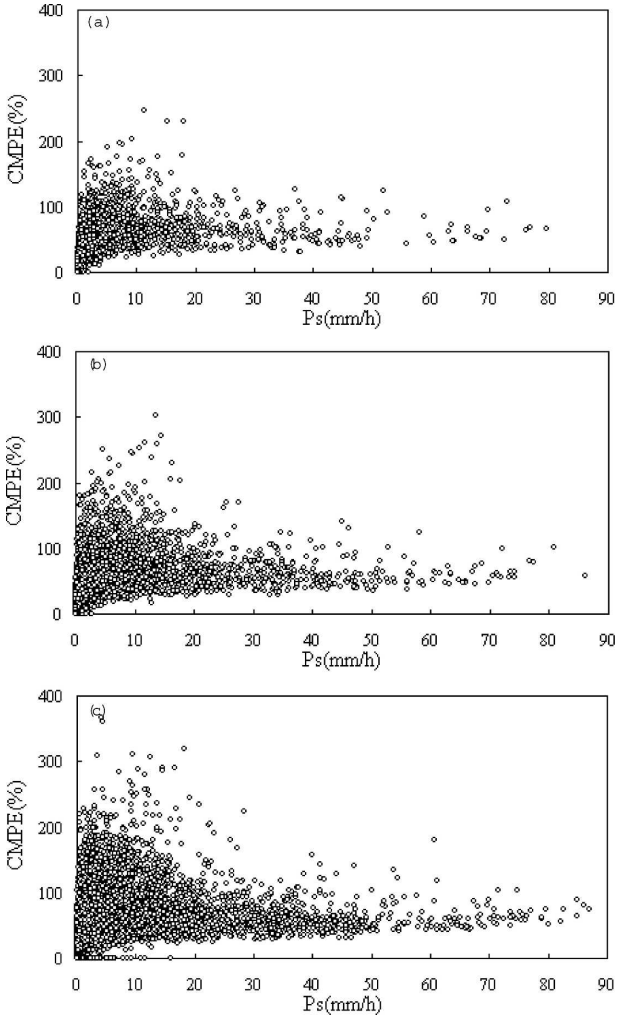

FIG. 11. Same as in Fig. 6 but for the MM5 simulation of Typhoon Nari (in 2001) averaged within (a) 118 km^2 (24 points), (b) 59 km^2 (12 points), and (c) 30 km^2 (6 points). Results are for ocean points only.

additional hydrometeor converging into the atmospheric column would make the precipitation efficiency larger. When the hydrometeor convergence becomes the dominant term in the cloud budget, the CMPE can be larger than 100% as found in light rain conditions (<5 mm h^{-1}). On the other hand, a loss of clouds due to hydrometeors diverging out to the neighboring columns would make the CMPE smaller. This occurs mostly in heavy rain conditions (>5 mm h^{-1}). The 3D simulation of a heavy-precipitating typhoon generally supports the 2D results except that the threshold value is ~20–30 mm h^{-1}.

The current study of precipitation efficiency provides a basis for further investigations of large-scale environments that determine the precipitation efficiency. The suggested effect of hydrometeor transport on precipitation efficiency is just one example. It is obvious that the determination of precipitation efficiency in the numerical models requires a cloud-resolving resolution to explicitly simulate cloud-microphysical processes. Therefore, prognostic parameterization schemes of clouds should be included in the numerical models for a better quantitative precipitation estimate/forecast (QPE/F).

Acknowledgments. The authors thank Prof. M. Zhang at the State University of New York at Stony Brook for his TOGA COARE forcing data, and two anonymous reviewers for their constructive comments. This research has been supported by the National Sciences Council in Taiwan under Grants NSC 91-2111-M-008-027 and NSC 93-2119-M-008-010-AP1.

REFERENCES

Arakawa, A., and W. H. Schubert, 1974: Interaction of a cumulus cloud ensemble with the large-scale environment, Part I. *J. Atmos. Sci.,* **31,** 674–701.

Betts, A. K., 1986: A new convective adjustment scheme. Part I: Observational and theoretical basis. *Quart. J. Roy. Meteor. Soc.,* **112,** 677–691.

——, and M. J. Miller, 1986: A new convective adjustment scheme. Part II: Single column tests using GATE wave, BOMEX, ATEX, and artic air-mass data sets. *Quart. J. Roy. Meteor. Soc.,* **112,** 693–709.

Doswell, C. A., III, H. E. Brooks, and R. A. Maddox, 1996: Flash flood forecasting: An ingredients-based methodology. *Wea. Forecasting,* **11,** 560–581.

Ferrier, B. S., J. Simpson, and W.-K. Tao, 1996: Factors responsible for precipitation efficiencies in midlatitude and tropical squall simulations. *Mon. Wea. Rev.,* **124,** 2100–2125.

Grell, G. A., 1993: Prognostic evaluation of assumptions used by cumulus parameterizations. *Mon. Wea. Rev.,* **121,** 764–787.

——, J. Dudhia, and D. R. Stauffer, 1994: A description of the fifth-generation Penn State/NCAR Mesoscale Model. NCAR Tech. Note NCAR/TN-398+STR, 121 pp.

Hsie, E.-Y., R. D. Farley, and H. D. Orville, 1980: Numerical simulation of ice-phase convective seeding. *J. Appl. Meteor.,* **19,** 950–977.

Kain, J. S., and J. M. Fritsch, 1993: Convective parameterization for mesoscale model: The Kain–Fritsch scheme. *The Representation of Cumulus Convection in Numerical Models, Meteor. Monogr.,* No. 46, Amer. Meteor. Soc. 165–177.

Krueger, S. K., Q. Fu, K. N. Liou, and H.-N. S. Chin, 1995: Improvement of an ice-phase microphysics parameterization for use in numerical simulations of tropical convection. *J. Appl. Meteor.,* **34,** 281–287.

Kuo, H. L., 1965: On formation and intensification of tropical cyclones through latent heat release by cumulus convection. *J. Atmos. Sci.,* **22,** 40–63.

——, 1974: Further studies of the parameterization of the influence of cumulus convection on large-scale flow. *J. Atmos. Sci.,* **31,** 1232–1240.

Li, X., C.-H. Sui, K.-M. Lau, and M.-D. Chou, 1999: Large-scale forcing and cloud–radiation interaction in the tropical deep convective regime. *J. Atmos. Sci.,* **56,** 3028–3042.

——, ——, and ——, 2002a: Interaction between tropical convection and its embedding environment: An energetics analysis of a 2D cloud resolving simulation. *J. Atmos. Sci.,* **59,** 1712–1722.

——, ——, and ——, 2002b: Precipitation efficiency in the tropical deep convective regime: A 2-D cloud resolving modeling study. *J. Meteor. Soc. Japan,* **80,** 205–212.

——, ——, and ——, 2002c: Dominant cloud microphysical processes in a tropical oceanic convective system: A 2D cloud resolving modeling study. *Mon. Wea. Rev.,* **130,** 2481–2491.

Lin, Y.-L., R. D. Farley, and H. D. Orville, 1983: Bulk parameterization of the snow field in a cloud model. *J. Climate Appl. Meteor.,* **22,** 1065–1092.

Lipps, E. B., and R. S. Hemler, 1986: Numerical simulation of deep tropical convection associated with large-scale convergence. *J. Atmos. Sci.,* **43,** 1796–1816.

Liu, Y., D.-L. Zhang, and M. K. Yau, 1997: A multiscale numerical study of Hurricane Andrew (1992). Part I: Explicit simulation and verification. *Mon. Wea. Rev.,* **125,** 3073–3093.

Lord, S. J., H. E. Willoughby, and J. M. Piotrowicz, 1984: Role of a parameterized ice-phase microphysics in an axisymmetric, nonhydrostatic tropical cyclone model. *J. Atmos. Sci.,* **41,** 2836–2848.

Manabe, S., and R. F. Strickler, 1964: Thermal equilibrium of the atmosphere with a convective adjustment. *J. Atmos. Sci.,* **21,** 361–385.

Reisner, J., R. J. Rasmussen, and R. T. Bruitjes, 1998: Explicit forecasting of supercooled liquid water in winter storms using the MM5 mesoscaled model. *Quart. J. Roy. Meteor. Soc.,* **124,** 1071–1107.

Rutledge, S. A., and P. V. Hobbs, 1983: The mesoscale and microscale structure and organization of clouds and precipitation in mid-latitude cyclones. VIII: A model for the "seeder-feeder" process in warm-frontal rainbands. *J. Atmos. Sci.,* **40,** 1185–1206.

——, and ——, 1984: The mesoscale and microscale structure and organization of clouds and precipitation in mid-latitude cyclones. XII: A diagnostic modeling study of precipitation development in narrow cold-frontal rainbands. *J. Atmos. Sci.,* **41,** 2949–2972.

Soong, S. T., and Y. Ogura, 1980: Response of tradewind cumuli to large-scale processes. *J. Atmos. Sci.,* **37,** 2035–2050.

——, and W.-K. Tao, 1980: Response of deep tropical cumulus clouds to mesoscale processes. *J. Atmos. Sci.,* **37,** 2016–2034.

Sui, C.-H., K.-M. Lau, W.-K. Tao, and J. Simpson, 1994: The tropical water and energy cycles in a cumulus ensemble model. Part I: Equilibrium climate. *J. Atmos. Sci.,* **51,** 711–728.

——, X. Li, and K.-M. Lau, 1998: Radiative-convective processes in simulated diurnal variations of tropical oceanic convection. *J. Atmos. Sci.,* **55,** 2345–2359.

——, and Coauthors, 2002: Typhoon Nari and Taipei Flood—A pilot meteorology–hydrology study. *Eos, Trans. Amer. Geophys. Union,* **83,** 265–270.

Tao, W.-K., and J. Simpson, 1993: The Goddard Cumulus Ensemble model. Part I: Model description. *Terr. Atmos. Oceanic Sci.,* **4,** 35–72.

——, ——, and M. McCumber, 1989: An ice-water saturation adjustment. *Mon. Wea. Rev.,* **117,** 231–235.

——, J. Samson, C.-H. Sui, S. Lang, J. Scala, B. Ferrier, M. D. Chou, and K. Pickering, 1993: Heating, moisture and water budgets in the convective and stratiform regions of tropical and mid-latitude squall lines: Their sensitivity to longwave radiation. *J. Atmos. Sci.,* **50,** 673–690.

——, D. Johnson, C.-L. Shie, and J. Simpson, 2004: The atmospheric energy budget and large-scale precipitation efficiency of convective systems during TOGA COARE, GATE, SCSMEX, and ARM: Cloud-resolving model simulations. *J. Atmos. Sci.,* **61,** 2405–2423.

Weisman, M. L., and J. B. Klemp, 1982: The dependence of numerically simulated convective storms on vertical wind shear and buoyancy. *Mon. Wea. Rev.,* **110,** 504–520.

Weller, R. A., and S. P. Anderson, 1996: Surface meteorology and air–sea fluxes in the western equatorial Pacific warm pool during TOGA COARE. *J. Climate,* **9,** 1959–1990.

Willoughby, H. E., H. L. Jin, S. J. Lord, and J. M. Piotrowicz, 1984: Hurricane structure and evolution as simulated by an axisymmetric, non-hydrostatic numerical model. *J. Atmos. Sci.,* **41,** 1169–1186.

Yang, M.-J., and H.-L. Huang, 2004: Precipitation processes associated with the landfalling Typhoon Nari (2001). *Extended Abstracts, 26th Conf. on Hurricanes and Tropical Meteorology,* Miami, FL, Amer. Meteor. Soc., 5A.3. [Available online at http://ams.confex.com/ams/26HURR/techprogram/paper_75490.htm.]

Zhang, M. H., and J. L. Lin, 1997: Constrained variational analysis of sounding data based on column-integrated budgets of mass, heat, moisture, and momentum: Approach and application to ARM measurements. *J. Atmos. Sci.,* **54,** 1503–1524.